J Solid State Electrochem (2012) 16:3643–3649
DOI 10.1007/s10008-012-1797-1

ORIGINAL PAPER

A broad pore size distribution mesoporous SnO_2 as anode for lithium-ion batteries

Konda Shiva · M. S. R. N. Kiran · U. Ramamurty · S. Asokan · Aninda J. Bhattacharyya

Received: 15 May 2012 / Revised: 9 June 2012 / Accepted: 12 June 2012 / Published online: 4 July 2012

Abstract We demonstrate here that mesoporous tin dioxide (abbreviated M-SnO_2) with a broad pore size distribution can be a prospective anode in lithium-ion batteries. M-SnO_2 with pore size ranging between 2 and 7.5 nm was synthesized using a hydrothermal procedure involving two different surfactants of slightly different sizes, and characterized. The irreversible capacity loss that occurs during the first discharge and charge cycle is 890 mAh g^{-1}, which is smaller than the 1,010-mAh g^{-1} loss recorded for mesoporous SnO_2 (abbreviated S-SnO_2) synthesized using a single surfactant. After 50 cycles, the discharge capacity of M-SnO_2 (504 mAh g^{-1}) is higher than that of S-SnO_2 (401 mAh g^{-1}) and solid nanoparticles of SnO_2 (abbreviated nano-SnO_2<4 mAh g^{-1}) and nano-SnO_2. Transmission electron microscopy revealed higher disorder in the pore arrangement in M-SnO_2. This, in turn imparts lower stiffness to M-SnO_2 (elastic modulus, $E_R \approx 14.5$ GPa) vis-a-vis S-SnO_2 ($E_R \approx 20.5$ GPa), as obtained using the nanoindentation technique. Thus, the superior battery performance of M-SnO_2 is attributed to its intrinsic material mechanical property. The fluidity of the internal microstructure of M-SnO_2 resulted in a lower degree of aggregation of Sn particles compared to S-SnO_2 and nano-SnO_2 structural stabilization and long-term cyclability.

Electronic supplementary material The online version of this article (doi:10.1007/s10008-012-1797-1) contains supplementary material, which is available to authorized users.

K. Shiva · A. J. Bhattacharyya (✉)
Solid State and Structural Chemistry Unit,
Indian Institute of Science,
Bangalore 560012, India
e-mail: aninda_jb@yahoo.com

S. Asokan
Department of Instrumentation and Applied Physics,
Indian Institute of Science,
Bangalore 560012, India

M. S. R. N. Kiran · U. Ramamurty
Department of Materials Engineering, Indian Institute of Science,
Bangalore 560012, India

Introduction

The high-energy storage capacity attainable in the case of lithium-ion batteries (LiBs) has made them the frontrunners for several electrical energy and power applications [1–4]. To meet the increasing demand for high energy and performance along with safety, considerable research efforts are being invested towards the development of new electrodes and electrolytes for LiB. One such strategy is the realization of non-carbonaceous alternative anodes to graphite with the main goal of developing anodes which can reversibly store Li at a voltage higher than that for graphite (≈0.1 V) so that the safety of the cell is enhanced and yet display high energy and rate capability. Among a large number of potential alternative negative materials, tin oxide (SnO_2) is the most promising owing to its high theoretical reversible capacity of 782 mAh g^{-1}, which is more than twice that of commercial graphite (372 mAh g^{-1}) [5–9]. Lithium storage in SnO_2 occurs via a two-step reaction [9–11]. The first step involves the irreversible conversion of SnO_2 to Sn and Li_2O. The second step is a reversible one involving alloying reaction of Li with Sn ($Li_{4.4}Sn$, i.e., 4.4 Li/mol of SnO_2). The first step is responsible for the severe irreversible capacity loss (≈800 mAh g^{-1}) which is primarily due to the formation of electrochemically inactive Li_2O. In addition, practical application of SnO_2 as an anode material is mainly hindered by the drastic volume changes (≈300 %) that occur during Li uptake and release from Sn resulting in severe grain degradation [12, 13]. The loss of contact between individual grains blocks e^-/Li^+ percolation leading to a severe fade in capacity. To overcome these problems and to enhance

cyclability of the electrode, composites of solid particles of SnO_2 with electronic conductors such as carbon or other conductive materials are produced [8, 14–16]. The carbon acts as electronic wires making electronic transport more efficient. Final properties of the carbon–SnO_2 composite, however, depend on complex optimization procedures with regard to type and content of carbon [17–20]. Additionally, there is no guarantee that contact between the disintegrating particles is retained during successive cycling. Further, the carbon does not always completely aid in the control of aggregation of tin crystallites during charge/discharge cycles which is also a key factor contributing to capacity fade. In light of this, utilizing SnO_2 particles with a porous internal structure (with pore size≈few nanometers) appears to be an effective and superior approach towards minimization of detrimental effects of volume changes and particle aggregation on cycling. Apart from much reduced length scales which lead to faster transport of e^-/Li^+ and higher Li^+ storage, the pores provide ample empty spaces to absorb drastic volume changes occurring during the alloying/dealloying reaction.

Mesoporous materials have demonstrated considerable potential in various fields especially in electrochemical energy generation and storage [6, 21, 22]. Majority of the reports, however, are on mesoporous materials synthesized using one structure-directing agent such as a surfactant, which results in a narrow pore size distribution and a periodic arrangement of the pores. We demonstrate here that a periodic arrangement of multisized pores in a mesoporous configuration is more beneficial than single-sized pores and possesses superior physicochemical properties. A facile method comprising a mixture of two surfactants of similar sizes was employed to synthesize high-surface-area SnO_2 with a broad pore size distribution. The Li battery performance and mechanical properties measured using nanoindentation techniques of M-SnO_2 are presented vis-a-vis SnO_2 synthesized using a single surfactant (abbreviated S-SnO_2). Effectiveness of the microstructure on the efficiency of the reversible electrochemical reaction was using ex situ X-ray diffraction and transmission electron microscopy.

Experimental section

Preparation of mesoporous S-SnO_2 and M-SnO_2

Hydrated tin chloride ($SnCl_4{\cdot}5H_2O$, Sigma-Aldrich) was used as the precursor for synthesis of mesoporous SnO_2. Single-pore SnO_2, i.e., S-SnO_2, was prepared using cetyl trimethylammonium bromide (abbreviated CTAB; SDFINE, India) whereas cetrimide (abbreviated CT; SRL, Mumbai) was additionally used for synthesis of multipore SnO_2 (M-SnO_2). For the synthesis of S-SnO_2, 2.6 g of CTAB, and for M-SnO_2, 2.6 g mixture of CTAB $(C_{16}H_{33})N(CH_3)_3Br$ and CT $(C_{14}H_{29})N(CH_3)_3Br$ (1:1 *w*/*w*), were mixed with 30 ml deionized water. The aqueous mixtures were stirred until a homogenous solution was obtained. Following this, NH_4OH solution was added into the aqueous surfactant solution. The addition of an aqueous solution of $SnCl_4{\cdot}5H_2O$ (3 g $SnCl_4{\cdot}5H_2O$ in 50 ml distilled water) to the aqueous surfactant–NH_4OH mixture resulted in a white slurry. The mixture was stirred for 5 h, and the pH of the solution was maintained throughout between 6.0 and 7.0 using diluted NH_4OH solution. The stirred-clear solution was then transferred to a Teflon container housed inside in steel cylinder for the hydrothermal reaction at 80 °C for 48 h. The final white product was collected by centrifugation, washed several times with distilled water, dried at ambient temperature, and additionally calcined (350 °C) in for removal of surfactants. The nonporous SnO_2 nanoparticles (abbreviated SnO_2) were synthesized under identical experimental conditions without any surfactants.

Material characterization

The structure of SnO_2 powder samples was investigated using powder X-ray diffraction (XRD, Philips X'Pert Pro diffractometer; CuK_α radiation, λ=1.5418 Å, voltage of 40 kV; current=30 mA) using over 2θ=20°–80°. The particle morphology of SnO_2 samples was characterized by transmission electron microscope (TEM, FEI Technai T20; operated at an accelerating voltage of 200 kV). For TEM studies, the samples were dispersed in ethanol, ultrasonicated, and dropped onto a carbon-coated Cu grid prior to the microscopy experiments. Specific surface area (Brunauer–Emmett–Teller or BET) and pore size distribution (Barrett–Joyner–Halenda or BJH) were obtained from nitrogen adsorption–desorption isotherms (Belsorp). For these studies, the samples were outgassed at 140 °C for 6 h before the measurement. The nanoindentation experiments were performed on the Triboindenter (Hysitron, Minneapolis, USA) with a Berkovich tip of radius 100 nm (with an in situ imaging capability) on 5-mm-thick and 10-mm-diameter pellets of S-SnO_2 and M-SnO_2. A loading/unloading rate of 0.5 mN s^{-1} and a hold time of 10 s at peak load (=5 mN) were employed for the nanoindentation test and the resulting load (P) vs. depth of penetration (h) of the indenter were recorded. The resolutions for P and h are 1 nN and 0.2 nm, respectively. A minimum of ten indentations per sample were made, all in load-controlled mode. The impressions of the indentations were captured, immediately after unloading, using the same indenter tip in the scanning mode. To determine the thermal stability of the SnO_2 samples, a thermogravimetric analysis (Mettler Toledo) was performed by heating the sample in air from room temperature (≈25 °C) to 650 °C at a heating rate of 5 °C/min.

For electrochemical measurements, a slurry of S-/M-/nano-SnO_2 (active) material was prepared with carbon black (Alfa Aesar) and PVDF (Kynarflex) in the weight ratio of

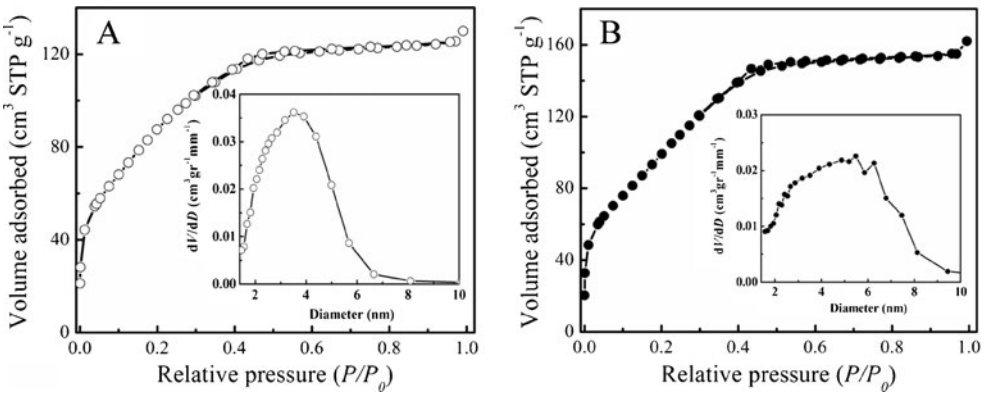

Fig. 1 N_2 adsorption–desorption isotherms for **a** S-SnO_2 and **b** M-SnO_2. *Inset*: pore size distributions for **a** S-SnO_2 and **b** M-SnO_2

75:15:10 in *N*-methyl-pyrrolidone to form a homogeneous slurry. This was then cast on a copper foil (Alfa Aesar, thickness=0.05 mm) and dried in vacuum at 120 °C for 12 h. The weight of active materials varied between 1.5 and 2.0 mg for each cell. All electrochemical measurements were performed at room temperature (25 °C). Galvanostatic charge/discharge cycling (Arbin Instruments, MSTAT) were performed in laboratory Swagelok™ cells with Li (Aldrich) as anode, Whatman glass fiber as separator, and 1 M $LiPF_6$ in ethylene carbonate (Aldrich) and dimethyl carbonate (DMC, Aldrich) (1:1 *w*/*w*) as electrolyte. All cell assembly was done at 25 °C in a glove box (MBraun) under argon (H_2O, <0.1 ppm). The galvanostatic cycling was performed in the voltage range of 0.005 and 1.5 V (vs. Li^+/Li). For ex situ XRD measurements, a requisite number of galvanostatic charge/discharge cycles were performed at a constant current density of 90 mA g^{-1}. Following the battery cycling, the cells were disassembled inside the argon-filled glove box, and the (charged/discharged) electrodes were cleaned several times with DMC. They were dried and stored in the glove box until further use.

Results and discussion

Figure 1 shows the nitrogen adsorption–desorption isotherms of mesoporous S-SnO_2 and M-SnO_2 samples prepared using the procedure described in the "Preparation of

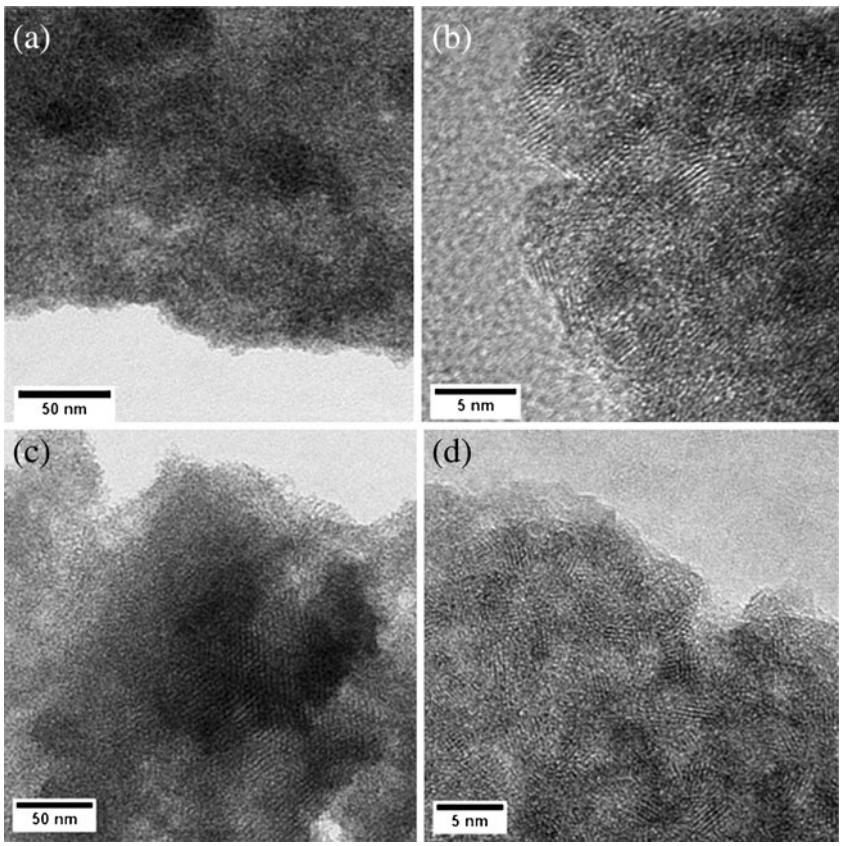

Fig. 2 TEM images of S-SnO_2 (**a** and **b**) and M-SnO_2 (**c** and **d**) before start of cycling

mesoporous S-SnO2 and M-SnO2" section. Both S-SnO_2 and M-SnO_2 exhibit type IV isotherm signifying a mesoporous internal structure. The BET surface areas were 330 $m^2\ g^{-1}$ (pore volume=0.48 gcm^{-3}) and 315 $m^2\ g^{-1}$ (pore volume=0.28 gcm^{-3}) for M-SnO_2 and S-SnO_2, respectively. The pore size distribution was estimated using the BJH method. For S-SnO_2, the peak of the distribution was observed at 3.7 nm (Fig. 1a, inset). For M-SnO_2, the pore size distribution was broad (2–7.5 nm) with the peak of the distribution lying in the range of 4 to 6 nm (Fig. 1b, inset). The wide pore size distribution (including the broad maximum) observed in the case of M-SnO_2 sample results as a consequence of usage of similar-sized surfactants during the synthesis (CTAB: $(C_{16}H_{33})N(CH_3)_3Br$; cetrimide: $(C_{14}H_{29})N(CH_3)_3Br$). It is supposed that this is a better approach than employing surfactants with widely varying sizes as the latter would result in much lower surface area (even compared to S-SnO_2) and lower lithium storage capacity (*vide infra*). In this regard we had synthesized mesoporous M-SnO_2 using Pluronic P-123 surfactant and CTAB instead of cetrimide and CTAB. The cycling performance of mesoporous SnO_2 was not satisfacory (not discussed here).

Mesoporosity of S-SnO_2 and M-SnO_2 was also confirmed by TEM (Fig. 2a–d). Due to a wide pore size distribution, the M-SnO_2 micrographs (Fig. 2c, d) appear more distinct and more disordered as compared to the S-SnO_2 (Fig. 2a, b) before cycling. Detailed pore arrangement in S-SnO_2 and M-SnO_2 samples could not be ascertained directly from the micrographs. High-resolution TEM images showed lattice fringes with individual crystallite sizes of 3–4 nm and a porous shell wall. The crystallite size estimates from TEM are in close proximity to the average crystallite size of 4 nm (both cases) estimated from XRD using the Scherrer equation. Thus, findings from N_2 adsorption–desorption, XRD, and TEM measurements are in agreement with each other.

Figure 3 shows the galvanostatic 1st, 2nd, and 50th charge–discharge cycles of S-SnO_2 and M-SnO_2. Lithium storage in SnO_2 takes place through the following steps:

$$SnO_2 + 4Li^+ + 4e^- \rightarrow Sn + 2Li_2O \quad (1)$$

$$Li^+ + e^- + \text{electrolyte} \rightarrow \text{solid electrolyte interface, SEI(Li)} \quad (2)$$

$$Sn + xLi^+ + xe - \rightleftarrows Li_xSn (0 \le \times \le 4.4) \quad (3)$$

Reactions as per Eqs. (1) and (2) are irreversible and are responsible for the large capacity loss observed between the first discharge and charge cycle [12, 23, 24]. The reaction depicted in Eq. (3), i.e., the alloying reaction, is reversible

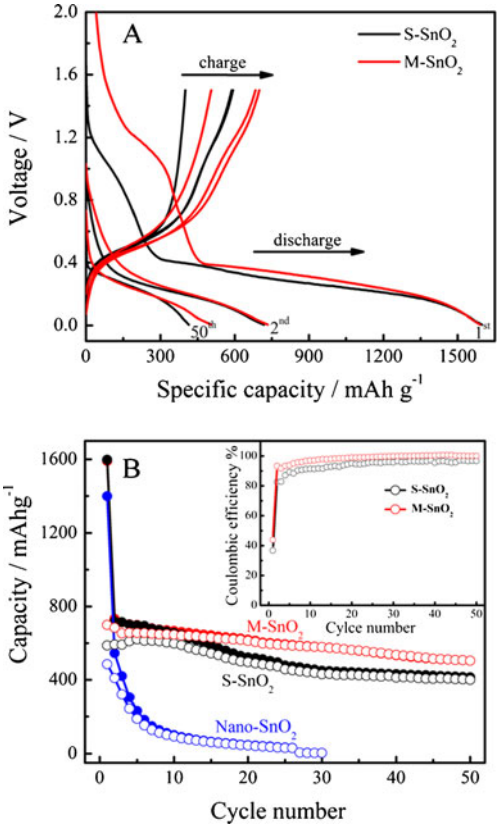

Fig. 3 **a** Galvanostatic charge–discharge cycles of S-SnO_2 and M-SnO_2 at room temperature. **b** Capacity vs. cycle number of nano-SnO_2, S-SnO_2, and M-SnO_2 nanoparticles at current density of 90 mA g^{-1}

and theoretically amounts to 830 mAh g^{-1}. The occurrence of all these reactions was confirmed via cyclic voltammetry (supporting information Fig. S1). The first discharge cycle capacities are 1,598 and 1,590 mAh g^{-1} for S-SnO_2 and M-SnO_2, respectively. Following the first cycle charge, capacities of S-SnO_2 and M-SnO_2 decrease to 588 and 699 mAh g^{-1}, respectively. Thus, the irreversible capacity (IRC) loss after the first cycle is lower in the case of M-SnO_2 (890 mAh g^{-1}) as compared to S-SnO_2 (1,009 mAh g^{-1}).

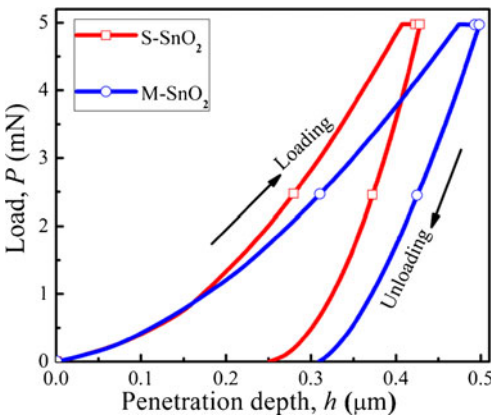

Fig. 4 Representative load (P)–displacement (h) curves obtained from S-SnO_2 and M-SnO_2

The large IRC loss between the first discharge and first charge is mainly attributed to the formation of Li_2O and SEI. The evidence for the formation of Li_2O ($SnO_2+4Li^+ + 4e^- \rightarrow Sn+2Li_2O$) and SEI is obtained from the cyclic voltammetry (supporting information Fig. 1). The M-SnO_2 exhibits a high coulombic efficiency of ~93 % in the second cycle as compared to 83 % noted for S-SnO_2 and much higher than solid nanometer-sized SnO_2 particles (75 %). Following the first charge cycle (or second discharge cycle), the capacity is observed to be fairly stable for both S-SnO_2 and M-SnO_2 as shown in Fig. 3. After 50 cycles (Fig. 3b), the discharge capacities of S-SnO_2 and M-SnO_2 are 401 and 504 mAh g^{-1}, respectively. This corresponds to a capacity retention of 72 % (M-SnO_2) and 68 % (S-SnO_2) of their first charge capacities, and the coulombic efficiencies are 97 and 100 %. Thus, the capacity values for S-SnO_2 and M-SnO_2 are much higher than that of commercial graphite with a reported value of ~300 mAh g^{-1} [25]. In the case of nano-SnO_2, the first cycle discharge capacity was also high (1,398 mAh g^{-1}). However, with an increasing cycle number, it decreased rapidly, and by the 30th discharge cycle, the capacity was only 4 mAh g^{-1} [14, 26–29]. This rapid decrease is attributed to drastic deterioration in the grain morphology (cracking followed by pulverization) leading to poor cyclability. On the other hand, good cycling performance of S-SnO_2 and M-SnO_2 is attributed to mesoporosity, which supposedly makes the matrix compliant and thus accommodates cyclic volumetric strains better. The broad pore size distribution in M-SnO_2 appears to impart better cyclic performance as compared to S-SnO_2. To ascertain this, we have examined the mechanical properties of the SnO_2 particles through nanoindentation.

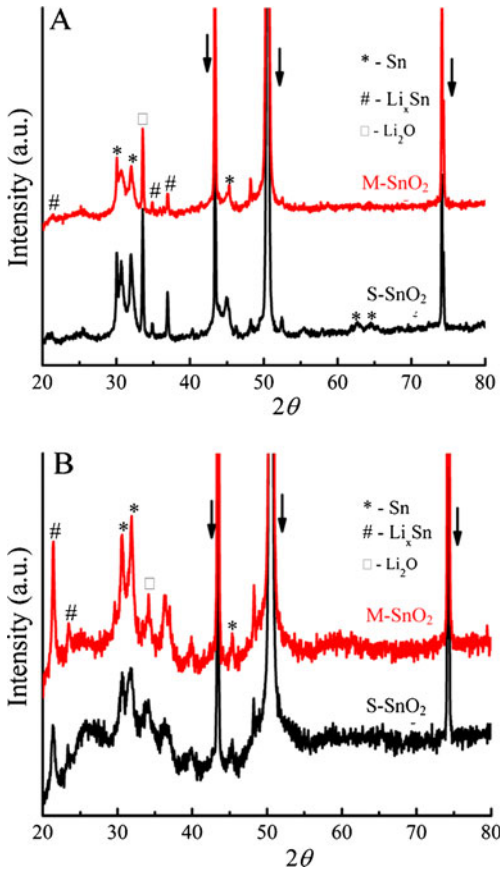

Fig. 5 XRD pattern of S-SnO_2 and M-SnO_2 after **a** the first discharge and **b** after the first charge cycle

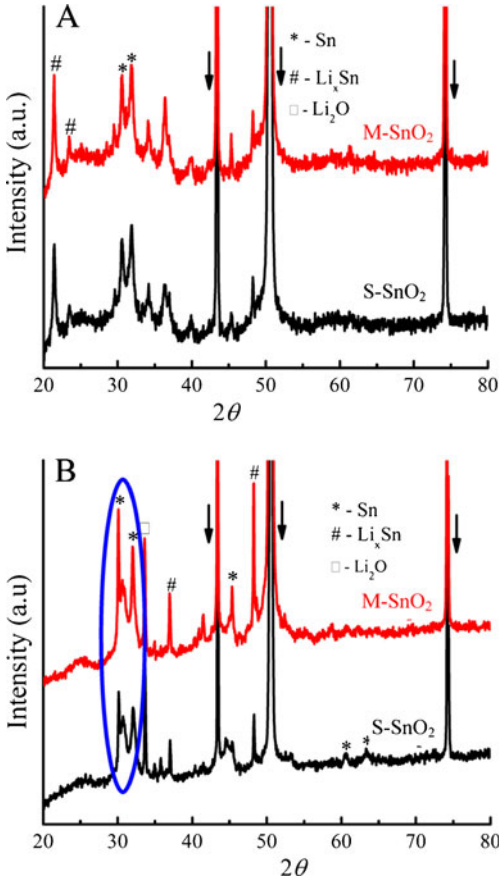

Fig. 6 XRD pattern of S-SnO_2 and M-SnO_2 after 5 cycles (**a**) and after 30 cycles (**b**)

Figure 4 shows representative load, *P*, vs. depth of penetration, *h*, curves for the two materials of interest. It is clear that there is no signature of pop-ins in the loading part of the *P*–*h* curves for both the samples indicating that the plastic deformation mechanism is homogeneous in nature. While the maximum depth of penetration of the indenter at the peak load of 5 N for the S-SnO_2 is ~450 nm, it is 500 nm for the M-SnO_2 sample. This indicates lower resistance to the indenter by the M-SnO_2 compared to S-SnO_2. The elastic moduli, *E*, were determined using the Oliver–Pharr method [30], which utilized the contact stiffness, *S*, determined from the slope (=d*P*/d*h*) of the upper portion (initial stages) of the unloading part of the curve. The above method has been used because no pile-up or sink-in and fracture are observed in the post-indent images of the indents (not shown here).

While the hardness of S-SnO_2 is 1.15±0.08 GPa, it is 0.81±0.05 GPa for M-SnO_2. The estimated values of *E* are 20.51±0.95 for S-SnO_2 and 14.48±1.02 GPa for M-SnO_2. The data indicates that M-SnO_2 is substantially more compliant and softer as compared to S-SnO_2. This is possibly due to the disordered arrangement of the pores in M-SnO_2 which makes less resistant to applied deformation. This property is expected to make the M-SnO_2 microstructure more efficient in managing volume changes occurring during lithium alloying/dealloying reactions which in turn lead to better cyclability and higher storage capacity. The particle cracking and miscontacts between them get reduced for M-SnO_2 in comparison to S-SnO_2.

Figures 5 and 6 show the ex situ XRD patterns of the S-SnO_2 and M-SnO_2 electrodes as a function of charge and discharge cycles. This figure shows the assignments of various phases in the sample. The before-cycling data (Fig. S2) could be indexed to the rutile phase (ICDD 41-1445). XRD data were collected following the 1st discharge (Fig. 5a), 1st charge (Fig. 5b), 5th charge (Fig. 6a), and 30th charge (Fig. 6b) cycles. The S-SnO_2 and M-SnO_2 after the first discharge consist of the alloy phases Li_xSn (Li_2Sn_5 and Li_7Sn_2), Sn (tetragonal) [10–12, 31], and inactive Li_2O. The existence of Li_xSn following completion of charge suggests that all the lithium could not be completely removed from Sn even after charging to 1.5 V. The Li_xSn phase was observed to exist even following the fifth charge cycle.

Even though no extra Li_xSn peaks were observed, Sn is observed to be present only in small amounts. The non-visibility of the extra Li_xSn peaks could be attributed to their existence in amorphous form. In M-SnO_2, particle cracking was less compared to S-SnO_2 due to better accommodation of volume changes occurring during successive charge/discharge cycling. This is evident from the ex situ XRD (Fig. 6b, blue circle). In the case of M-SnO_2 after 30 cycles, the change in particle size (≈5.1 nm) is less as compared to that before cycling (≈5 nm). For S-SnO_2, after the 30th cycle, the particle size decreases to ≈3.6 nm compared to that before cycling (≈5 nm). We show that Sn atoms aggregate into larger clusters as the materials are discharged and charged many times (up to 30 cycles) but that the cluster size finally reaches a stable size. The Sn particles have a lower degree of aggregation in M-SnO_2 compared to S-SnO_2. This leads to an efficient alloying/dealloying reaction. It is already known in the literature [32], in the case of nano-SnO_2, that aggregation was much higher and capacity faded rapidly within a few cycles.

Conclusions

We have demonstrated here the importance of the presence of pores and their distribution on the electrochemical performance of SnO_2. Mesoporous SnO_2 with a broad pore size distribution (M-SnO_2) is convincingly demonstrated to be a viable alternative to the usual monodispersed mesoporous material (S-SnO_2). This is based on the superior battery performance of M-SnO_2 compared to S-SnO_2. We suppose that there still exists room for additional improvements following optimization of electrode synthesis parameters and binder/conductive additives. We envisage that this strategy will also prove to be beneficial if adopted for Sn or, as a matter of fact, for any anode or cathode materials displaying considerable volume changes as a result of reaction with lithium.

Acknowledgments The authors thank H.B. Rajendra (SSCU, IISc) for discussions and E.A. Anumol (MRC, IISc) for the TEM facility. MSRNK thanks The University Grants Commission for a Dr. D.S. Kothari Postdoctoral Fellowship. KS acknowledges CSIR for SRF. AJB thanks DST, Govt. of India, for financial support, and CEN, IISc., for the glove box facility.

References

1. Tarascon JM, Armand M (2001) Nature 414:359–367
2. Wang B, Bates JB, Hart FX, Sales BC, Zuhr RA, Robertson JD (1996) J Electrochem Soc 143:3203–3213
3. Bruce PG, Scrosati B, Tarascon J-M (2008) Angew Chem Int Ed 47:2930–2946
4. Ji X, Lee KT, Nazar LF (2009) Nat Mater 8:500–506
5. Li N, Martin CR (2001) J Electrochem Soc 148:A164
6. Wang C, Zhou Y, Ge M, Xu X, Zhang Z, Jiang JZ (2009) J Am Chem Soc 132:46–47
7. Winter M, Besenhard JO, Spahr ME, Novák P (1998) Adv Mater 10:725–763
8. Lou XW, Li CM, Archer LA (2009) Adv Mater 21:2536–2539
9. Idota Y, Kubota T, Matsufuji A, Maekawa Y, Miyasaka T (1997) Science 276:1395
10. Courtney IA, Dahn JR (1997) J Electrochem Soc 144:2045–2052
11. Courtney IA, Dahn JR (1997) J Electrochem Soc 144:2943–2948
12. Winter M, Besenhard JO (1999) Electrochim Acta 45:31
13. Paek S-M, Yoo E, Honma I (2008) Nano Lett 9:72–75
14. Park S-K, Yu S-H, Pinna N, Woo S, Jang B, Chung Y-H, Cho Y-H, Sung Y-E and Piao Y (2012) J Mater Chem
15. Park M-S, Kang Y-M, Kim J-H, Wang G-X, Dou S-X, Liu H-K (2008) Carbon 46:35–40
16. Lou XW, Chen JS, Chen P, Archer LA (2009) Chem Mater 21:2868–2874
17. Sun X, Liu J, Li Y (2006) Chem Mater 18:3486–3494
18. Wen Z, Wang Q, Zhang Q, Li J (2007) Adv Funct Mater 17:2772–2778
19. Chen JS, Cheah YL, Chen YT, Jayaprakash N, Madhavi S, Yang YH, Lou XW (2009) J Phys Chem C 113:20504–20508
20. Kim JG, Nam SH, Lee SH, Choi SM, Kim WB (2011) ACS Appl Mater Interfaces 3:828–835
21. Demir-Cakan R, Hu Y-S, Antonietti M, Maier J, Titirici M-M (2008) Chem Mater 20:1227–1229
22. Deng D, Lee JY (2008) Chem Mater 20:1841–1846
23. Besenhard JO, Yang J, Winter M (1997) J Power Sources 68:87–90
24. Mao O, Dunlap RA, Dahn JR (1999) J Electrochem Soc 146:405–413
25. Flandrois S, Simon B (1999) Carbon 37:165–180

26. Yong W, Minghong W, Zheng J, Jim Yang L (2009) Nanotechnology 20:345704
27. Xu W, Canfield NL, Wang D, Xiao J, Nie Z, Zhang J-G (2010) J Power Sources 195:7403–7408
28. Kang J-H, Paek S-M, Choy J-H (2012) Chem Commun 48:458–460
29. Shiva K, Asokan S, Bhattacharyya AJ (2011) Nanoscale 3:1501–1503
30. Oliver WC, Pharr GM (1992) J Mater Res 7:1564–1580
31. Kim C, Noh M, Choi M, Cho J, Park B (2005) Chem Mater 17:3297–3301
32. Courtney IA, McKinnon WR, Dahn JR (1999) J Electrochem Soc 146:59–68